JACS
JOURNAL OF THE AMERICAN CHEMICAL SOCIETY
pubs.acs.org/JACS
Article

Interfacial Metal Nanocluster Conduits Direct Charge Transfer for Record Unassisted Solar Water Splitting

Yurou Song,[○] Yuye Jiao,[○] Xin Liu,[○] Jinbo Liu, Dingfeng Jin, Wanying Guo, Siyu Jiao, Shijie Lu, Guanghao Chen, Biao Yang, Licheng Sun, Jungang Hou,* and Bin Liu*

Cite This: https://doi.org/10.1021/jacs.6c01306

ABSTRACT: Photoelectrochemical (PEC) water splitting offers one of the most promising solutions for sustainable solar-to-chemical fuel conversion. However, sluggish charge migration across the photoelectrode interface fundamentally limits the PEC efficiency. Herein, we design and engineer an atomic-scale interfacial charge conduit by inserting metal nanoclusters between the cocatalyst and semiconductor. The distinct work-function differences among the cocatalyst, metal nanoclusters, and semiconductor induce interfacial band bending, enabling the selective, directional transport of photogenerated carriers from the semiconductor to the cocatalyst. Particularly, bismuth (Bi) nanoclusters synthesized through a universal laser-induced *in situ* growth strategy on 29 distinct bismuth-based semiconductors induce the formation of metal/semiconductor Schottky junctions and directionally steer electron migration into the semiconductor conduction band while effectively suppressing electron−hole recombination. Benefiting from the Bi nanoclusters and CoFe cocatalyst, the large-area (3×3 cm^2) earth-abundant CoFe/Bi/$BiVO_4$ photoanode achieves a photocurrent of 26 mA at 1.1 V versus RHE, maintaining stable performance for 600 h. For practical application, an all-oxide-semiconductor tandem PEC device combining a CoFe/Bi/$BiVO_4$ photoanode and a Pt/TiO_2/Ga_2O_3/Cu_2O/CuO photocathode records an unassisted 4.8% solar-to-hydrogen conversion efficiency under AM 1.5G light illumination for 70 h. This work demonstrates the atomic-scale engineering of interfacial charge conduits for high-efficiency solar energy conversion.

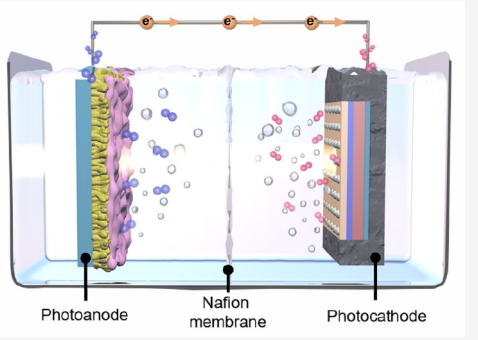

INTRODUCTION

Solar energy-driven photoelectrochemical (PEC) water splitting provides a sustainable and renewable approach for green hydrogen production.[1,2] However, various semiconductor photoelectrodes, such as Si,[3] TiO_2,[4] α-Fe_2O_3,[5] $BiVO_4$,[6] Ta_3N_5,[7] and WO_3,[8] present intrinsic drawbacks with high defect-state densities, sluggish surface reaction kinetics, and restricted carrier mobilities,[9,10] hindering solar-to-hydrogen conversion efficiency. To address these problems, metal/semiconductor interface engineering has emerged as an effective strategy.[11−14]

In conventional PEC devices, metal/semiconductor contacts typically form Schottky or ohmic junctions, depending on the work-function difference.[15−17] However, in practice, surface states and interfacial defects often pin the Fermi level of semiconductor photoelectrodes, rendering the Schottky junction insensitive to the metal work function. In general, work-function difference compensation is governed by surface-state charges rather than space charges (Figure 1a).[18,19] Consequently, the nature of metal/semiconductor contacts and their potential barriers significantly affect the band structure of the semiconductor and thus charge transfer. Noble metals (e.g., Au, Pt, and Pd) are commonly employed in interface construction through atomic layer deposition, wet chemical reduction, or photoreduction.[20−23] Yet, precisely regulating interface contact and enabling directional charge transport remain challenging.

Herein, we design an atomic-scale interfacial charge conduit to induce directional photogenerated charge transfer via metal nanoclusters inserted between the cocatalyst and semiconductor in an integrated photoanode. Notably, the work-function difference of the cocatalyst, metal nanoclusters, and semiconductor results in band bending at the photoanode surface, expediting charge transfer. Concurrently, the cocatalyst promotes the extraction of photogenerated holes and accelerates water oxidation kinetics. In particular, we develop a universal laser-induced *in situ* growth method to deposit metallic Bi nanoclusters on the surface of Bi-based semiconductor photoanodes (29 distinct Bi-based semiconductor photoanodes are studied). A large-area (3×3 cm^2) CoFe/Bi/$BiVO_4$ nanoarray photoanode with incorporated Bi nano-

Received: January 19, 2026
Revised: February 21, 2026
Accepted: March 3, 2026

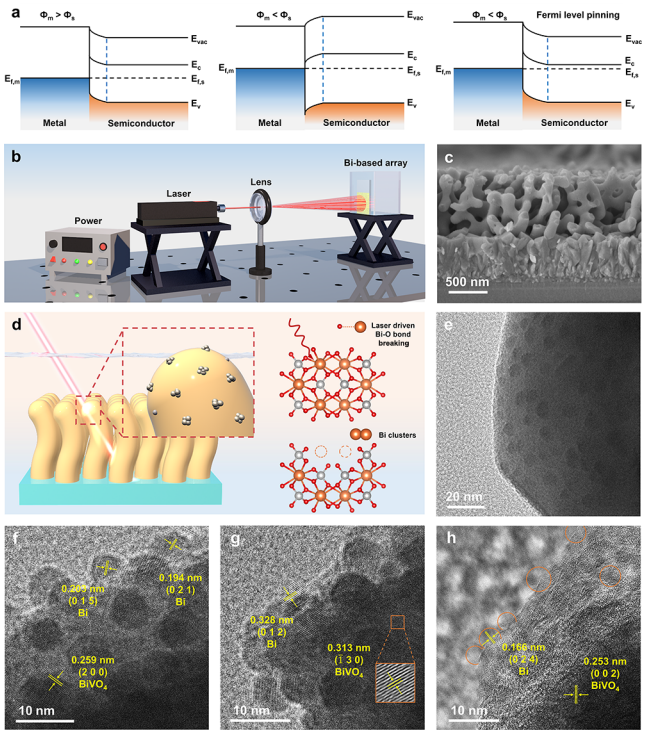

Figure 1. Laser-induced *in situ* growth of Bi nanoclusters. (a) Band diagrams showing the interactions between different metals and semiconductors. (b) Schematic illustration showing the experimental apparatus. (c) High-resolution cross-sectional SEM image of Bi/$BiVO_4$. (d) Schematic illustration of the *in situ* grown Bi nanoclusters on a $BiVO_4$ nanoarray. TEM images of Bi/$BiVO_4$ prepared after (e, f) 20 min and (g) 30 min of laser irradiation at a laser intensity of 550 mW cm^{-2} and after (h) 20 min of laser irradiation at a laser intensity of 250 mW cm^{-2}.

clusters is able to deliver a photocurrent of 26 mA at 1.1 V versus reversible hydrogen electrode (RHE) for over 600 h. When coupled with a Pt/TiO_2/Ga_2O_3/Cu_2O/CuO photocathode, the tandem PEC device records a 4.8% solar-to-hydrogen conversion efficiency under AM 1.5G light illumination for 70 h. This work opens a new direction for interfacial charge transfer engineering to achieve high-efficiency solar energy conversion.

RESULTS AND DISCUSSION

Laser-Induced *In Situ* Growth of Bi Nanoclusters

Bi nanoclusters were formed on the surface of the $BiVO_4$ photoanode by a laser-induced *in situ* growth method (Figure 1b). During the growth process, the Bi−O bond was partially broken under infrared laser irradiation at a wavelength of 1064 nm, facilitating the *in situ* growth of Bi nanoclusters (Figure 1d). No characteristic peaks of metallic Bi are observed in the XRD pattern due to the low content of Bi nanoclusters (Figure S1). All diffraction peaks for $BiVO_4$ and Bi/$BiVO_4$ nanoarrays can be assigned to monoclinic $BiVO_4$ (JCPDS PDF #14-0688).[24] The scanning electron microscopy (SEM) images of $BiVO_4$ and Bi/$BiVO_4$ (laser intensity of 550 mW cm^{-2} for 10 min) in Figures 1c and S2 present no discernible morphological differences, but some Bi nanoclusters are observable in Bi/$BiVO_4$ from the transmission electron microscopy (TEM) measurements shown in Figure S3. Extending the laser irradiation time to 20 min increased the number of Bi nanoclusters (~6 nm) (Figure S6), which were homogeneously dispersed on the surface of the $BiVO_4$ nanoarray. The lattice fringes of 0.194 and 0.203 nm observed in the high-resolution TEM image correspond to the (021) and (015) crystal planes of Bi clusters (JCPDS PDF #44-1246) (Figure 1e,f). Further extending the laser irradiation time to 30 min caused the aggregation of Bi nanoclusters (Figure 1g). On the other hand, lowering the laser intensity to 250 mW cm^{-2} decreased both the density and size of the Bi nanoclusters on the $BiVO_4$ surface (Figure 1h), while prolonging the laser irradiation time and increasing the laser intensity led to agglomeration of the Bi nanoclusters as well as damage to the $BiVO_4$ surface (Figure S4). Consequently, the size and density of Bi nanoclusters can be properly controlled on the $BiVO_4$ surface by adjusting the laser intensity and irradiation time. Compared with conventional Bi deposition methods, the laser-induced *in situ* growth method offers a much more convenient approach to grow high-density and uniformly sized Bi nanoclusters on $BiVO_4$ (Figure S5).

A Universal Strategy to Grow Bi Nanoclusters on Bi-Based Semiconductors

To examine the generalizability of the laser-induced *in situ* growth method for depositing Bi nanoclusters, we fabricated 29 different Bi-based oxide and oxyhalide semiconductor nanoarrays. TEM characterizations reveal the uniform formation of Bi nanoclusters on the surfaces of all 29 Bi-based semiconductors (Figures 2 and S7−S38), indicating a universal strategy for the laser-induced method to grow Bi nanoclusters.

The structural symmetry dependent Bi−O bonding characteristics fundamentally govern Bi nanocluster formation. p-$BiVO_4$ exhibits a higher Bi−O binding energy than its n-type counterpart, attributed to the enhanced structural symmetry.[25,26] As a result, the average size of the Bi nanoclusters synthesized on p-$BiVO_4$ (~5.0 nm) is smaller than that of the Bi nanoclusters synthesized on n-$BiVO_4$ (~6.0 nm) (Figures 2m and S34). This trend extends to Aurivillius-phase Bi_2MO_6 (M = W, Mo, Cr), where the Bi−O binding energy scales with the M-site electronic configuration: Bi_2WO_6 > Bi_2MoO_6 > Bi_2CrO_6. The interaction of Cr−O in Bi_2CrO_6 weakens the bonding energy of the Bi−O bond.[27−29] This results in a larger Bi nanocluster size on Bi_2CrO_6 than on Bi_2WO_6 (Figures 2o,p and S9−S11). Notably, van der Waals layered BiOX (X = Cl, Br, I) displays a Bi−O binding energy inversely correlating with the X^- ionic radius and electronegativity.[30−32] Enhanced chemical bonding networks and strengthened van der Waals interactions are found to increase the Bi−O bond stability, thus suppressing Bi nanocluster growth (Figures 2a,i,j and S29−S31). The findings presented above reveal the widespread applicability of the laser-induced *in situ* growth method for forming Bi nanoclusters on Bi-based semiconductors.

Laser-Induced *In Situ* Growth Mechanism of Bi Nanoclusters

The laser-induced *in situ* growth process may involve an "excitation-removal" sequence initiated by a 1064 nm far-infrared laser (Figure 3a). Multiphoton absorption under far-infrared laser excitation could lead to an optical resonance effect.[33] In the presence of ethylene glycol as a reducing agent, this effect facilitates the escape of Bi atoms from the surface. Taking n-$BiVO_4$, p-$BiVO_4$, Bi_2WO_6, and BiOCl as representative examples, high-resolution X-ray photoelectron spectroscopy (XPS) analysis of the Bi 4f spectra reveals the presence of

https://doi.org/10.1021/jacs.6c01306
J. Am. Chem. Soc. XXXX, XXX, XXX−XXX

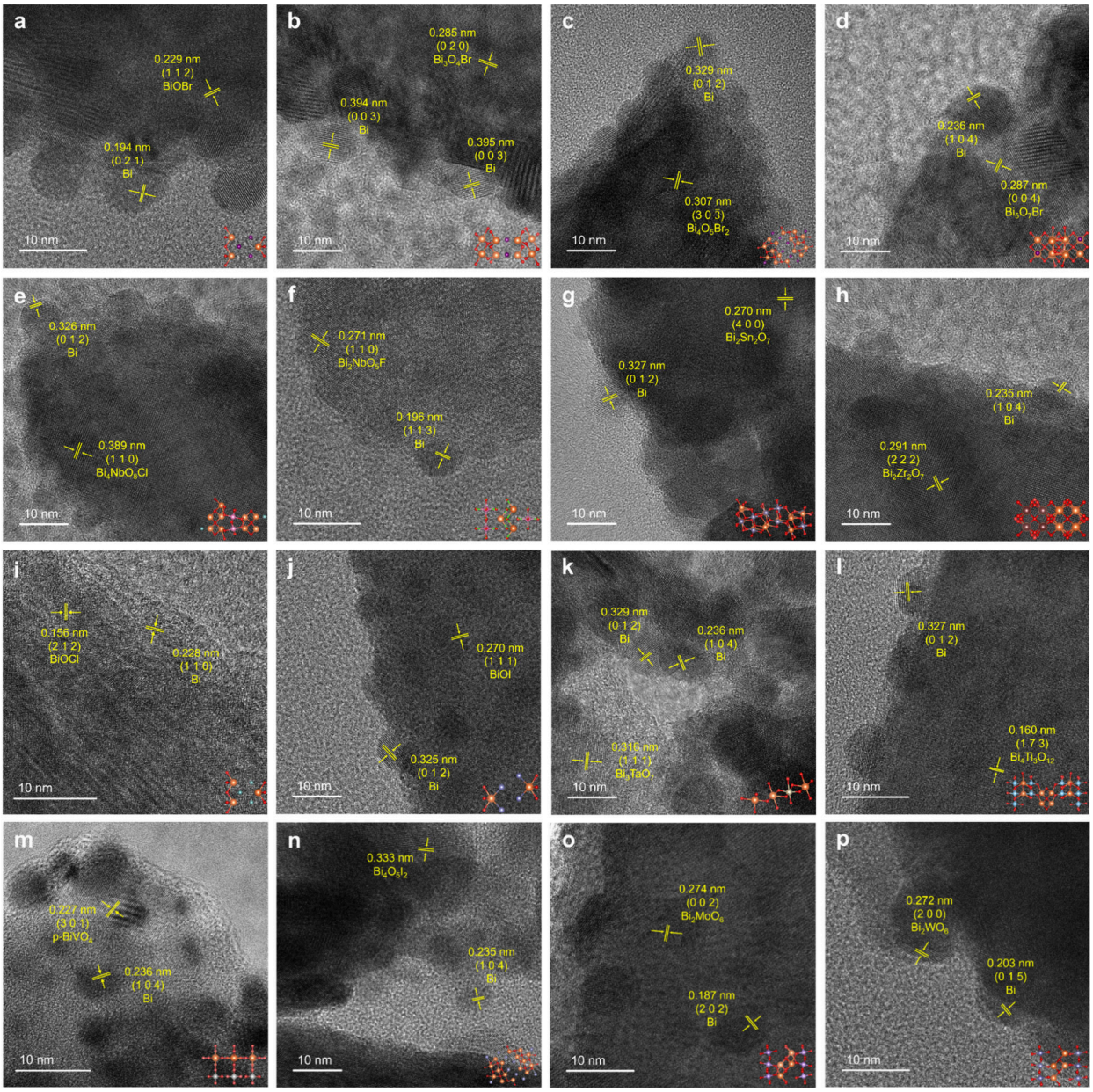

Figure 2. A universal strategy for forming Bi nanoclusters on Bi-based semiconductors. HRTEM images of (a) Bi/BiOBr, (b) Bi/Bi_3O_4Br, (c) Bi/$Bi_4O_5Br_2$, (d) Bi/Bi_5O_7Br, (e) Bi/Bi_4NbO_8Cl, (f) Bi/Bi_2NbO_5F, (g) Bi/$Bi_2Sn_2O_7$, (h) Bi/$Bi_2Zr_2O_7$, (i) Bi/BiOCl, (j) Bi/BiOI, (k) Bi/Bi_3TaO_7, (l) Bi/$Bi_4Ti_3O_{12}$, (m) Bi/p-$BiVO_4$, (n) Bi/$Bi_4O_5I_2$, (o) Bi/Bi_2MoO_6, and (p) Bi/Bi_2WO_6 prepared by laser-induced *in situ* growth at a laser intensity of 550 mW cm^{-2} for 20 min.

Bi^0 on these Bi-based semiconductors after the laser-induced *in situ* growth process (Figures S39−S42). As shown in Figure 3c,e,g,i, two characteristic peaks are observed in the O 1s XPS spectra. The peak centered at ∼530 eV is assigned to lattice oxygen. The peak at ∼531.5 eV is attributed to surface hydroxyl species or defect associated oxygen environments, which are commonly correlated with oxygen vacancy related surface states. The formation of oxygen vacancy related defects was further validated by electron paramagnetic resonance (EPR) spectroscopy. As shown in Figure 3d,f,h,j, the EPR signals at g = 2.003 correspond to electrons trapped at oxygen vacancies.[40,41] As schematically illustrated in Figure 3b, oxygen atoms can be more readily removed at the Bi nanocluster/Bi-based semiconductor interface to generate oxygen defects.[34−39] Figure 3k−n shows the oxygen vacancy formation process over n-$BiVO_4$, p-$BiVO_4$, Bi_2WO_6, and BiOCl during laser-induced *in situ* growth of Bi nanoclusters.

PEC Performance

To elucidate the role of metal nanoclusters in charge transport across the metal/semiconductor interface, we compared the work-function evolution, band structure modification, and charge carrier dynamics in Bi/$BiVO_4$, Au/$BiVO_4$, Pt/$BiVO_4$, and Pd/$BiVO_4$ systems with those of Bi, Au, Pt, and Pd nanoclusters. Ultraviolet photoelectron spectroscopy (UPS) reveals an increased apparent work function in $BiVO_4$ for all M/$BiVO_4$ (M = Au, Pt, Pd) due to their higher intrinsic work functions relative to that of $BiVO_4$ (Figures S43−S46). Pt/$BiVO_4$ exhibits the largest increase, consistent with the highest work function of Pt.[42−45] However, owing to the low intrinsic work function of Bi, the apparent work function of $BiVO_4$

https://doi.org/10.1021/jacs.6c01306
J. Am. Chem. Soc. XXXX, XXX, XXX−XXX

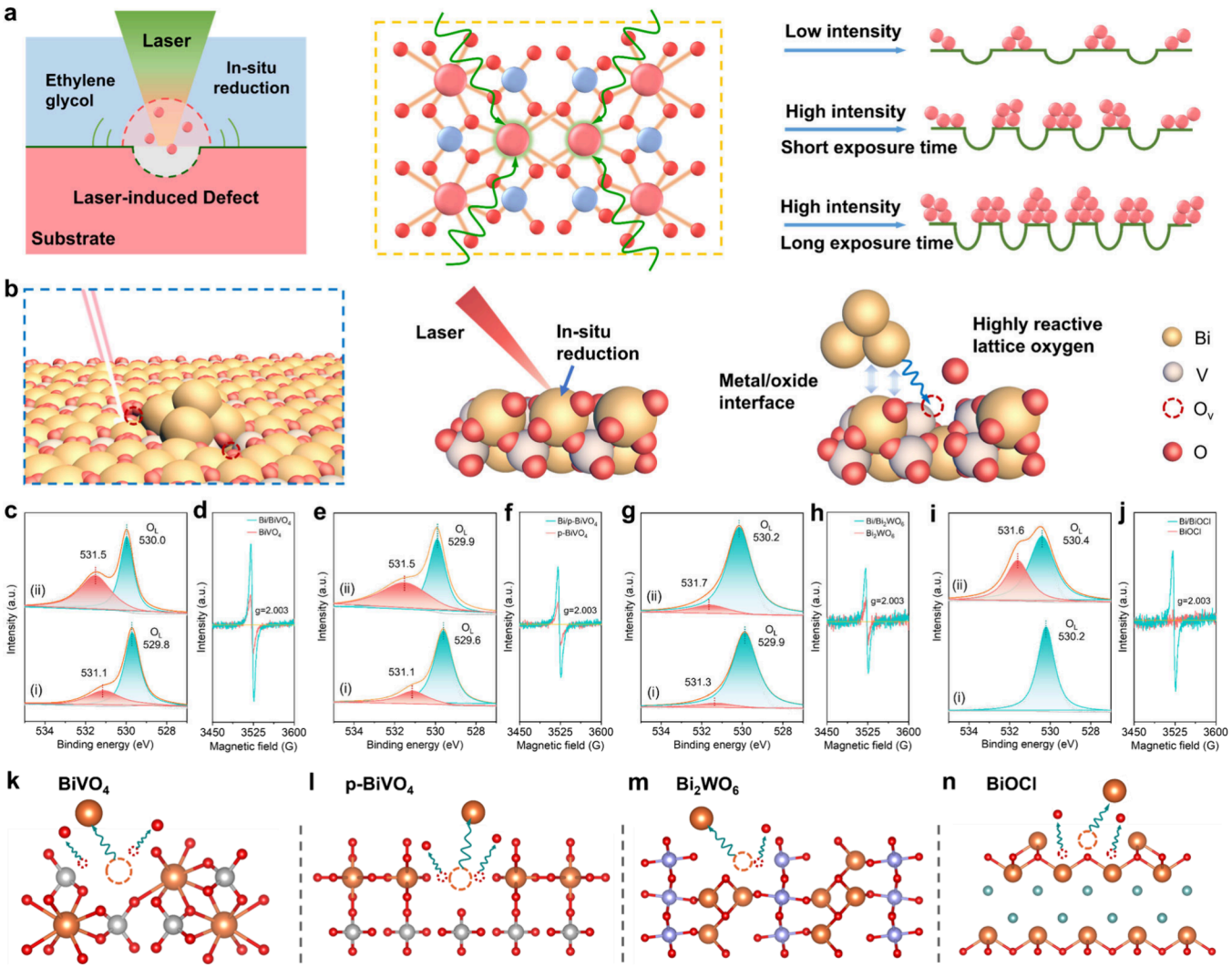

Figure 3. Laser-induced *in situ* growth mechanism of Bi nanoclusters. (a) Schematic illustration showing laser-induced *in situ* synthesis of Bi nanoclusters. (b) Schematic illustration showing the oxygen vacancy formation mechanism. High-resolution O 1s XPS spectra and EPR signals recorded over (c, d) Bi/$BiVO_4$, (e, f) Bi/p-$BiVO_4$, (g, h) Bi/Bi_2WO_6, and (i, j) Bi/BiOCl in comparison with pristine semiconductors. Structural illustration showing the formation process of oxygen vacancies on (k) $BiVO_4$, (l) p-$BiVO_4$, (m) Bi_2WO_6, and (n) BiOCl.

increases marginally in Bi/$BiVO_4$ (Figure S47), and the electrons can be transferred to the conduction band of $BiVO_4$ through Bi nanoclusters.

Moreover, the charge carrier dynamics in metal/$BiVO_4$ were probed. To enhance hole extraction for water oxidation, a CoFe-MOF cocatalyst (CoFe) was deposited onto the metal/$BiVO_4$ substrates (Figures S48−S53). The photoluminescence (PL) spectrum of CoFe/Bi/$BiVO_4$ displays the lowest PL intensity (Figure S54) in comparison to CoFe/Au/$BiVO_4$, CoFe/Pd/$BiVO_4$, and CoFe/Pt/$BiVO_4$, revealing the suppressed radiative recombination in CoFe/Bi/$BiVO_4$. The overall recombination dynamics were further elucidated by time-resolved photoluminescence (TR-PL) and photoelectrochemical analyses. The TR-PL spectrum of CoFe/Bi/$BiVO_4$ shows a longer τ_2 value and average charge carrier lifetime (τ_{ave}) compared to CoFe/Au/$BiVO_4$ and CoFe/Pd/$BiVO_4$, indicating reduced recombination, whereas CoFe/Pt/$BiVO_4$ exhibits the shortest charge carrier lifetime, comparable to that of CoFe/$BiVO_4$ (Figures 4d and S55, Table S1). Mott−Schottky (M-S) measurements reveal an enhanced carrier concentration in CoFe/Bi/$BiVO_4$ (Figure S56 and Table S2). PEC measurements disclose negligible photocurrent enhancement for CoFe/Au/$BiVO_4$ and CoFe/Pd/$BiVO_4$ compared to CoFe/$BiVO_4$, with CoFe/Pt/$BiVO_4$ exhibiting an even slightly decreased photocurrent (Figure S57). Moreover, controlled experiments were conducted to elucidate the role of oxygen vacancy related defects. The results indicate that while Bi nanoclusters and oxygen vacancy related defects individually contribute to improved charge separation (Figures S58−S61), the superior performance of CoFe/Bi/$BiVO_4$ arises from their synergistic integration via the laser-induced *in situ* growth process, which enables uniformly dispersed Bi nanoclusters and the optimal interfacial defect environment that suppresses charge recombination and promotes selective electron transport. Taken together, the band alignment and charge transport mechanisms in metal/$BiVO_4$ and CoFe/metal/$BiVO_4$ are shown in Figures 4a−c and S62−S67. In detail, the incorporation of a CoFe cocatalyst with a higher work function than pristine $BiVO_4$ induces strong band bending at the semiconductor/cocatalyst interface. The enlarged space charge region and suppressed electron−hole recombination promote the extraction of photogenerated holes. Moreover, noble

https://doi.org/10.1021/jacs.6c01306
J. Am. Chem. Soc. XXXX, XXX, XXX−XXX

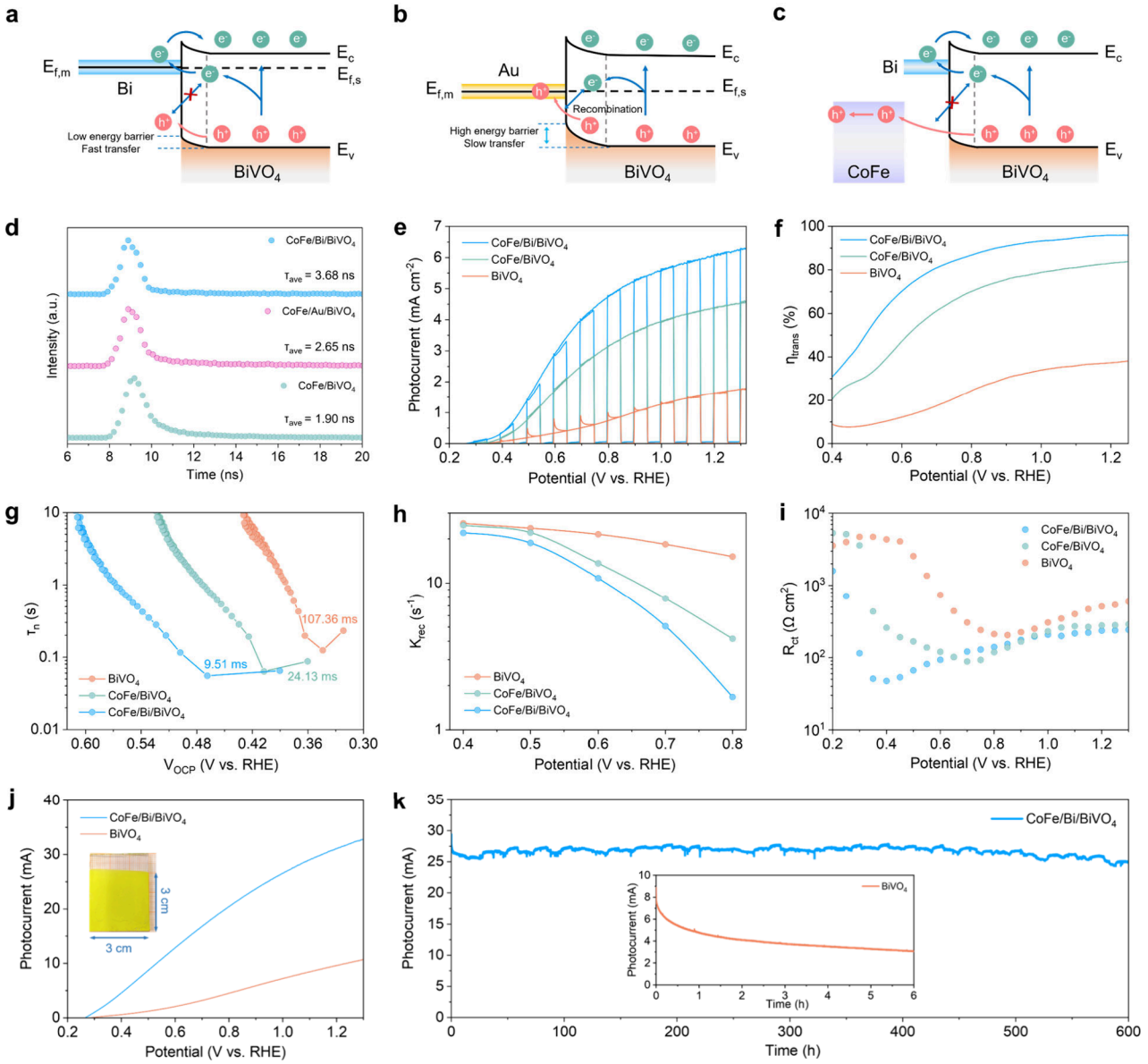

Figure 4. Band diagrams of (a) $Bi/BiVO_4$, (b) $Au/BiVO_4$, and (c)$CoFe/Bi/BiVO_4$. (d) TR-PL decay profiles of $CoFe/Bi/BiVO_4$, $CoFe/Au/BiVO_4$, and $CoFe/BiVO_4$. (e) LSV curves, (f) charge transfer efficiencies, (g) OCP-derived charge carrier lifetimes, (h) K_{rec} at various potentials extracted from IMPS measurements and (i) R_{ct} as a function of applied potential from PEIS for $BiVO_4$, $CoFe/BiVO_4$, and $CoFe/Bi/BiVO_4$. (j) LSV curves of the 3 × 3 cm^2 $BiVO_4$ and $CoFe/Bi/BiVO_4$ photoanodes. (k) $J-t$ curves of the 3 × 3 cm^2 $BiVO_4$ and $CoFe/Bi/BiVO_4$ photoanodes recorded at 1.1 V versus RHE.

metals such as Pt, Pd, and Au at the interlayer between the CoFe cocatalyst and $BiVO_4$ still serve as the hole transfer layer, adding negligible contribution toward boosting PEC performance owing to the excellent hole extraction capability of the CoFe cocatalyst. In contrast, Bi nanoclusters at the interlayer can facilitate electron transfer into the conduction band of $BiVO_4$ and thereby further suppress charge recombination, while the oxygen vacancy related defects facilitate assist charge separation and selective carrier transport. Thus, the synergistic contribution of Bi nanoclusters, oxygen vacancies, and CoFe cocatalysts in the $CoFe/Bi/BiVO_4$ photoanode significantly enhances the PEC performance.

By finely tuning the laser intensity and laser exposure time, the optimized $CoFe/Bi/BiVO_4$ photoanode (laser intensity: 550 mW cm^{-2}; laser exposure time: 20 min) with structural characterization shown in Figures S68−S73 reaches the highest photocurrent density of 6.07 mA cm^{-2} at 1.23 V versus RHE (Figures 4e, S74, and S75). Figures S76 and S77 display the incident photon-to-current conversion efficiency (IPCE) and applied bias photon-to-current conversion efficiency (ABPE) curves. The $CoFe/Bi/BiVO_4$ photoanode improves the charge separation and charge transfer efficiencies across the entire examined voltage range (Figures 4f and S78). From transient open-circuit potential (OCP) decay measurements (Figure S79), the charge transfer time in $CoFe/Bi/BiVO_4$ is found to be significantly reduced (Figure 4g). The intensity-modulated photocurrent spectra show a reduced charge recombination constant (K_{rec}) for $CoFe/Bi/BiVO_4$, accompanied by an increased charge transfer constant (K_{trans}) (Figures 4h, S80, and S81). The calculated charge diffusion coefficient (D_n) for $CoFe/Bi/BiVO_4$ (1.73×10^{-6} cm^2 s^{-1}) is more than twice that for $BiVO_4$ (6.69×10^{-7} cm^2 s^{-1}) (Figures S82 and S83). From

https://doi.org/10.1021/jacs.6c01306
J. Am. Chem. Soc. XXXX, XXX, XXX−XXX

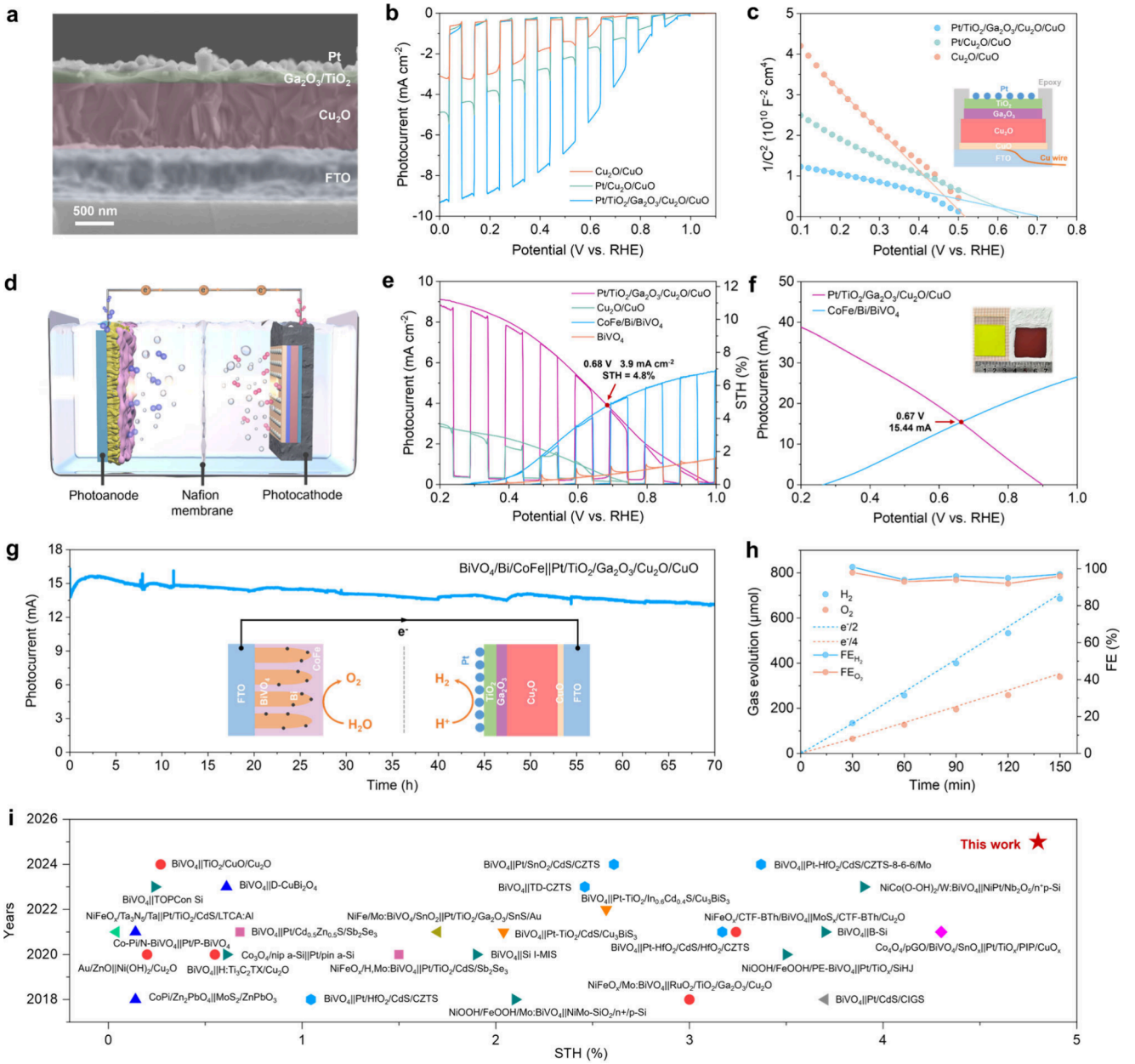

Figure 5. Unassisted PEC water splitting. (a) Cross-sectional SEM image of $Pt/TiO_2/Ga_2O_3/Cu_2O/CuO$. (b) LSV curves and (c) Mott−Schottky plots of Cu_2O/CuO, $Pt/Cu_2O/CuO$, and $Pt/TiO_2/Ga_2O_3/Cu_2O/CuO$. (d) Schematic illustration showing an unassisted PEC water splitting device. (e) Chopped current−potential curves of different $BiVO_4$-based photoanodes and Cu_2O-based photocathodes with a 1 × 1 cm^2 working area. (f) Current−potential curves of the $CoFe/Bi/BiVO_4$ photoanode and $Pt/TiO_2/Ga_2O_3/Cu_2O/CuO$ photocathode with a 3 × 3 cm^2 working area. (g) J−t curve showing the unassisted PEC water splitting device comprising a 3 × 3 cm^2 $CoFe/Bi/BiVO_4$ photoanode and a 3 × 3 cm^2 $Pt/TiO_2/Ga_2O_3/Cu_2O/CuO$ photocathode. Inset shows a schematic illustration. (h) Time dependent H_2 and O_2 evolution and the corresponding Faradaic efficiencies. (i) Performance comparison of unassisted PEC water splitting devices based on semiconductor photoelectrodes. Detailed information for each point is given in Table S3.

Figures 4i and S84−S86, the analyses of surface capacitance (C_s) and interface charge transfer resistance (R_{ct}) in the photoelectrochemical impedance spectroscopy (PEIS) spectra indicate that the C_s displays a typical Gaussian behavior for $BiVO_4$, which increases along with a decrease in R_{ct}, suggesting that the interfacial charge transfer of water oxidation occurs through surface states, in agreement with the cyclic voltammetry (CV) results shown in Figure S87.[46,47] In contrast, the $CoFe/Bi/BiVO_4$ photoanode exhibits a potential independent surface capacitance profile. This suggests the formation of a surface layer capacitance arising from the adsorption of oxy/hydroxyl species during the photocharging process, revealing a more complex surface state comprising both oxygen vacancies and adsorbed species.[48,49] The above collective analysis demonstrates that the greatly enhanced PEC performance of $CoFe/Bi/BiVO_4$ originates from the construction of a $Bi/BiVO_4$ Schottky electron-blocking layer and interfacial oxygen vacancies, which effectively inhibits electron−hole recombination and facilitates efficient charge separation; meanwhile, the CoFe cocatalyst accelerates hole extraction to promote the water oxidation kinetics.

https://doi.org/10.1021/jacs.6c01306
J. Am. Chem. Soc. XXXX, XXX, XXX−XXX

To assess the practical application potential, a 3 × 3 cm^2 CoFe/Bi/$BiVO_4$ photoanode was fabricated, which delivers an impressive photocurrent of 31.6 mA in comparison to 9.9 mA over a 3 × 3 cm^2 pristine $BiVO_4$ photoanode. Notably, the CoFe/Bi/$BiVO_4$ photoanode retains 93.8% of the initial photocurrent at 1.1 V versus RHE after 600 h of continuous operation (Figure 4j,k), indicating its excellent PEC stability. Furthermore, post characterization based on XRD, XPS, and Raman spectroscopy indicated minimal structural changes of the CoFe/Bi/$BiVO_4$ photoanode after PEC water oxidation reaction at 1.1 V versus RHE (Figures S88−S92).

Development of an Unassisted PEC Water Splitting Device

In the pursuit of practical solar-driven H_2 production, it is essential to develop an unassisted PEC device that can operate without external energy input. Such an unassisted PEC water splitting device can be constructed by coupling the CoFe/Bi/$BiVO_4$ photoanode to a suitable photocathode. Cu_2O-based photocathodes display a suitable Fermi level, and therefore, a Pt/TiO_2/Ga_2O_3/Cu_2O/CuO photocathode (Figure 5a) was fabricated, in which CuO acted as a back layer on fluorine-doped tin oxide (FTO) to enhance hole transfer; Ga_2O_3 was incorporated as a buffer layer to facilitate band alignment; TiO_2 served as a protective layer; and Pt nanoparticles acted as the cocatalyst for the hydrogen evolution reaction (Figures S93 and S94). Under AM 1.5G light illumination, the Pt/TiO_2/Ga_2O_3/Cu_2O/CuO photocathode obtains a maximum photocurrent density of 9.3 mA cm^{-2} at 0 V versus RHE (Figure 5b), displaying a p-type semiconductor characteristic (Figure 5c).

An unassisted PEC water splitting cell was fabricated by connecting the CoFe/Bi/$BiVO_4$ photoanode to the Pt/TiO_2/Ga_2O_3/Cu_2O/CuO photocathode by using a conductive wire (Figure 5d), in which solar light was irradiated from the photoanode to the photocathode. Figure 5e shows the chopped current−potential curves of the CoFe/Bi/$BiVO_4$ photoanode and the Pt/TiO_2/Ga_2O_3/Cu_2O/CuO photocathode with a 1 × 1 cm^2 working area, which intersect at a photocurrent density of 3.9 mA cm^{-2}, giving an estimated solar-to-hydrogen conversion efficiency of 4.8% for the unassisted PEC water splitting device.[50,51] This value is among the best values in the literature for unassisted PEC water splitting devices based on earth-abundant semiconductors (Figure 5i and Table S3). Importantly, this predicted operating point was further validated by a two-electrode measurement of the integrated tandem system under zero external bias, which exhibited a consistent bias-free photocurrent density (Figure S95). A larger working area (3 × 3 cm^2) CoFe/Bi/$BiVO_4$ + Pt/TiO_2/Ga_2O_3/Cu_2O/CuO device exhibits an operating photocurrent density of 15.44 mA (Figure 5f), which can be stably operated for 70 h without obvious photocurrent decay (Figure 5g). The decrease in photocurrent density and STH efficiency upon area enlargement can be mainly attributed to scale-up related factors, including increased series resistance, non-negligible ohmic losses in the electrolyte and current collectors, as well as more pronounced mass transport limitations and gas-bubble accumulation over a larger electrode surface.[52−54] The PEC reaction products were quantified by gas chromatography (GC), giving a stoichiometric ratio (2:1) of hydrogen to oxygen with nearly 100% Faradaic efficiencies (Figure 5h).

CONCLUSIONS

In summary, we have developed a simple laser-induced *in situ* growth method to construct Bi nanocluster interfacial charge conduits over Bi-based semiconductors, which effectively tailor band bending and steer directional charge transfer, greatly boosting the PEC performance. A 3 × 3 cm^2 CoFe/Bi/$BiVO_4$ photoanode delivers a photocurrent of 26 mA at 1.1 V versus RHE under AM 1.5G light illumination for over 600 h. Connecting to a Pt/TiO_2/Ga_2O_3/Cu_2O/CuO photocathode, the all-oxide-semiconductor tandem PEC device achieves unassisted water splitting under solar light irradiation, recording a 4.8% solar-to-hydrogen conversion efficiency. This work provides new insights for interfacial charge transfer engineering toward achieving high-efficiency solar energy conversion.

ASSOCIATED CONTENT

Supporting Information

The Supporting Information is available free of charge at https://pubs.acs.org/doi/10.1021/jacs.6c01306.

Detailed experimental procedures, photoelectrochemical measurements, XRD spectra, SEM and TEM images, XPS spectra, PEC tests, UV−vis spectra, and PEC data summary (PDF)

AUTHOR INFORMATION

Corresponding Authors

Jungang Hou − *State Key Laboratory of Fine Chemicals, Frontiers Science Center for Smart Materials Oriented Chemical Engineering, School of Chemical Engineering, Dalian University of Technology, Dalian 116024, P. R. China;* orcid.org/0000-0003-1896-2999; Email: jhou@dlut.edu.cn

Bin Liu − *Department of Materials Science and Engineering, City University of Hong Kong, Hong Kong SAR 999007, P. R. China; Department of Chemistry, Hong Kong Institute for Clean Energy Center (HKICE) & Center of Super-Diamond and Advanced Films (COSDAF), City University of Hong Kong, Hong Kong SAR 999077, P. R. China;* orcid.org/0000-0002-4685-2052; Email: bliu48@cityu.edu.hk

Authors

Yurou Song − *State Key Laboratory of Fine Chemicals, Frontiers Science Center for Smart Materials Oriented Chemical Engineering, School of Chemical Engineering, Dalian University of Technology, Dalian 116024, P. R. China*

Yuye Jiao − *State Key Laboratory of Fine Chemicals, Frontiers Science Center for Smart Materials Oriented Chemical Engineering, School of Chemical Engineering, Dalian University of Technology, Dalian 116024, P. R. China*

Xin Liu − *School of Materials Science and Engineering, Dalian University of Technology, Dalian 116024, P. R. China*

Jinbo Liu − *Key Laboratory of Chemical Lasers, Dalian Institute of Chemical Physics, Chinese Academy of Sciences, Dalian 116023, P. R. China*

Dingfeng Jin − *State Key Laboratory of Fine Chemicals, Frontiers Science Center for Smart Materials Oriented Chemical Engineering, School of Chemical Engineering, Dalian University of Technology, Dalian 116024, P. R. China*

https://doi.org/10.1021/jacs.6c01306
J. Am. Chem. Soc. XXXX, XXX, XXX−XXX

Wanying Guo − *State Key Laboratory of Fine Chemicals, Frontiers Science Center for Smart Materials Oriented Chemical Engineering, School of Chemical Engineering, Dalian University of Technology, Dalian 116024, P. R. China*

Siyu Jiao − *State Key Laboratory of Fine Chemicals, Frontiers Science Center for Smart Materials Oriented Chemical Engineering, School of Chemical Engineering, Dalian University of Technology, Dalian 116024, P. R. China*

Shijie Lu − *State Key Laboratory of Fine Chemicals, Frontiers Science Center for Smart Materials Oriented Chemical Engineering, School of Chemical Engineering, Dalian University of Technology, Dalian 116024, P. R. China*

Guanghao Chen − *State Key Laboratory of Fine Chemicals, Frontiers Science Center for Smart Materials Oriented Chemical Engineering, School of Chemical Engineering, Dalian University of Technology, Dalian 116024, P. R. China*

Biao Yang − *State Key Laboratory of Fine Chemicals, Frontiers Science Center for Smart Materials Oriented Chemical Engineering, School of Chemical Engineering, Dalian University of Technology, Dalian 116024, P. R. China*

Licheng Sun − *State Key Laboratory of Fine Chemicals, Frontiers Science Center for Smart Materials Oriented Chemical Engineering, School of Chemical Engineering, Dalian University of Technology, Dalian 116024, P. R. China; Center of Artificial Photosynthesis for Solar Fuels and Department of Chemistry, School of Science, Westlake University, Hangzhou 310024, P. R. China; Department of Chemistry, School of Engineering Sciences in Chemistry, Biotechnology and Health, KTH Royal Institute of Technology, 10044 Stockholm, Sweden;* orcid.org/0000-0002-4521-2870

Complete contact information is available at: https://pubs.acs.org/10.1021/jacs.6c01306

Author Contributions

○Y.S., Y.J., and X.L. contributed equally to this work.

Notes

The authors declare no competing financial interest.

■ ACKNOWLEDGMENTS

This work was supported by the National Key R&D Program of China (2023YFA1507101), National Natural Science Foundation of China (Nos. 22525201, 22372021, 224B2202, 225B2202), the Liaoning Binhai Laboratory (LBLD-2025-05), the Fundamental Research Funds for the Central Universities (Nos. DUT22LAB602, DUT24BK061, DUTZD25231, DUT25Z2779, DUT25Z3208, DUT25Z2734), Liaoning Joint Project for Technology Research and Development (2024JH2/102600047), the City University of Hong Kong Startup fund (9020003), ITF-RTH-Global STEM Professorship (9446006), and JC STEM lab of Advanced CO_2 Upcycling (9228005).

■ REFERENCES

(1) Wang, S.; Liu, G.; Wang, L. Crystal facet engineering of photoelectrodes for photoelectrochemical water splitting. *Chem. Rev.* **2019**, *119* (8), 5192−5247.

(2) He, Y.; Hamann, T.; Wang, D. Thin film photoelectrodes for solar water splitting. *Chem. Soc. Rev.* **2019**, *48* (7), 2182−2215.

(3) Teitsworth, T. S.; Hill, D. J.; Litvin, S. R.; Ritchie, E. T.; Park, J. S.; Custer, J. P., Jr.; Taggart, A. D.; Bottum, S. R.; Morley, S. E.; Kim, S.; McBride, J. R.; Atkin, J. M.; Cahoon, J. F. Water splitting with silicon p-i-n superlattices suspended in solution. *Nature* **2023**, *614* (7947), 270−274.

(4) Wu, S. M.; Wu, L.; Denisov, N.; Badura, Z.; Zoppellaro, G.; Yang, X. Y.; Schmuki, P. Pt single atoms on TiO_2 can catalyze water oxidation in photoelectrochemical experiments. *J. Am. Chem. Soc.* **2024**, *146* (24), 16363−16368.

(5) Li, J.; Chen, H.; Liu, S.; Wang, Y.; Wan, W.; Zhao, Y.; Triana, C. A.; Xu, Z.; Patzke, G. R. Accelerated recombination reaction through interfacial Fe(IV)═O accumulation on photoanode surfaces. *J. Am. Chem. Soc.* **2025**, *147* (25), 21492−21500.

(6) Kim, T. W.; Choi, K. S. Nanoporous $BiVO_4$ photoanodes with dual-layer oxygen evolution catalysts for solar water splitting. *Science* **2014**, *343* (6174), 990−994.

(7) Xiao, Y.; Feng, C.; Fu, J.; Wang, F.; Li, C.; Kunzelmann, V. F.; Jiang, C.-M.; Nakabayashi, M.; Shibata, N.; Sharp, I. D.; Domen, K.; Li, Y. Band structure engineering and defect control of Ta_3N_5 for efficient photoelectrochemical water oxidation. *Nat. Catal.* **2020**, *3* (11), 932−940.

(8) Wang, J.; Liu, K.; Liao, W.; Kang, Y.; Xiao, H.; Chen, Y.; Wang, Q.; Luo, T.; Chen, J.; Li, H.; Chan, T.-S.; Chen, S.; Pensa, E.; Chai, L.; Liu, F.; Jiang, L.; Liu, C.; Fu, J.; Cortés, E.; Liu, M. Metal vacancies in semiconductor oxides enhance hole mobility for efficient photoelectrochemical water splitting. *Nat. Catal.* **2025**, *8* (3), 229−238.

(9) Song, K.; Liu, H.; Chen, B.; Gong, C.; Ding, J.; Wang, T.; Liu, E.; Ma, L.; Zhao, N.; He, F. Toward efficient utilization of photogenerated charge carriers in photoelectrochemical systems: Engineering strategies from the atomic level to configuration. *Chem. Rev.* **2024**, *124* (24), 13660−13680.

(10) Kim, J. H.; Hansora, D.; Sharma, P.; Jang, J. W.; Lee, J. S. Toward practical solar hydrogen production-an artificial photosynthetic leaf-to-farm challenge. *Chem. Soc. Rev.* **2019**, *48* (7), 1908−1971.

(11) Esposito, D. V.; Levin, I.; Moffat, T. P.; Talin, A. A. H_2 evolution at Si-based metal-insulator-semiconductor photoelectrodes enhanced by inversion channel charge collection and H spillover. *Nat. Mater.* **2013**, *12* (6), 562−568.

(12) Xiao, Y.; Fu, J.; Pihosh, Y.; Karmakar, K.; Zhang, B.; Domen, K.; Li, Y. Interface engineering for photoelectrochemical oxygen evolution reaction. *Chem. Soc. Rev.* **2025**, *54* (3), 1268−1317.

(13) Xu, S.; Shen, Q.; Zheng, J.; Wang, Z.; Pan, X.; Yang, N.; Zhao, G. Advances in biomimetic photoelectrocatalytic reduction of carbon dioxide. *Adv. Sci.* **2022**, *9* (31), 2203941.

(14) Heo, J.; Segalina, A.; Kim, D.; Ahn, D.-S.; Oang, K. Y.; Park, S.; Kim, H.; Ihee, H. Ultrafast interfacial charge transfer initiates mechanical stress and heat transport at the Au-TiO_2 interface. *Adv. Sci.* **2024**, *11* (34), No. 2400919.

(15) Li, Q.; Wang, C.; Yao, H.; He, C.; Guo, C.; Hu, Y. Cocatalysts for photocatalysis: Comprehensive insight into interfacial charge transfer mechanism by energy band theory. *Coordin. Chem. Rev.* **2025**, *535*, 216652.

(16) Kwon, G.; Choi, Y.-H.; Lee, H.; Kim, H.-S.; Jeong, J.; Jeong, K.; Baik, M.; Kwon, H.; Ahn, J.; Lee, E.; Cho, M.-H. Interaction- and defect-free van der waals contacts between metals and two-dimensional semiconductors. *Nat. Electron.* **2022**, *5* (4), 241−247.

(17) Kawasaki, S.; Takahashi, R.; Yamamoto, T.; Kobayashi, M.; Kumigashira, H.; Yoshinobu, J.; Komori, F.; Kudo, A.; Lippmaa, M. Photoelectrochemical water splitting enhanced by self-assembled metal nanopillars embedded in an oxide semiconductor photoelectrode. *Nat. Commun.* **2016**, *7*, 11818.

(18) Jang, J.; Hong, J. P.; Kim, S.-J.; Ahn, J.; Yu, B.-S.; Han, J.; Lee, K.; Ha, A.; Yoon, E.; Kim, W.; Jo, S.; Ko, H. W.; Yoon, S. K.; Taniguchi, T.; Watanabe, K.; Baek, H.; Kim, D.-Y.; Lee, K.; Mun, S.; Lee, K. H.; Park, S.; Kim, K.; Song, Y. J.; Lee, S. A.; Kim, H. J.; Shim, J. W.; Wang, G.; Kang, J.-H.; Park, M.-C.; Hwang, D. K. Conductive-

bridge interlayer contacts for two-dimensional optoelectronic devices. *Nat. Electron.* **2025**, *8* (4), 298−308.
(19) Vilan, A.; Cahen, D. Chemical modification of semiconductor surfaces for molecular electronics. *Chem. Rev.* **2017**, *117* (5), 4624−4666.
(20) He, B.; Cao, Y.; Lin, K.; Wang, Y.; Li, Z.; Yang, Y.; Zhao, Y.; Liu, X. Strong interactions between Au nanoparticles and $BiVO_4$ photoanode boosts hole extraction for photoelectrochemical water splitting. *Angew. Chem., Int. Ed.* **2024**, *63* (23), No. e202402435.
(21) Shi, X.; Dai, C.; Wang, X.; Hu, J.; Zhang, J.; Zheng, L.; Mao, L.; Zheng, H.; Zhu, M. Protruding Pt single-sites on hexagonal $ZnIn_2S_4$ to accelerate photocatalytic hydrogen evolution. *Nat. Commun.* **2022**, *13* (1), 1287.
(22) Tayyebi, A.; Mehrotra, R.; Mubarok, M. A.; Kim, J.; Zafari, M.; Tayebi, M.; Oh, D.; Lee, S.-h.; Matthews, J. E.; Lee, S.-W.; Shin, T. J.; Lee, G.; Jaramillo, T. F.; Jang, S.-Y.; Jang, J.-W. Bias-free solar NH_3 production by perovskite-based photocathode coupled to valorization of glycerol. *Nat. Catal.* **2024**, *7* (5), 510−521.
(23) Li, X.; Mitchell, S.; Fang, Y.; Li, J.; Perez-Ramirez, J.; Lu, J. Advances in heterogeneous single-cluster catalysis. *Nat. Rev. Chem.* **2023**, *7* (11), 754−767.
(24) Wang, S.; Chen, P.; Yun, J. H.; Hu, Y.; Wang, L. An electrochemically treated $BiVO_4$ photoanode for efficient photoelectrochemical water splitting. *Angew. Chem., Int. Ed.* **2017**, *56* (29), 8500−8504.
(25) Kim, J. H.; Lee, J. S. Elaborately modified $BiVO_4$ photoanodes for solar water splitting. *Adv. Mater.* **2019**, *31* (20), No. 1806938.
(26) Liang, X.; Wang, P.; Tong, F.; Liu, X.; Wang, C.; Wang, M.; Zhang, Q.; Wang, Z.; Liu, Y.; Zheng, Z.; Dai, Y.; Huang, B. Bias-free solar water splitting by tetragonal zircon $BiVO_4$ nanocrystal photocathode and monoclinic scheelite $BiVO_4$ nanoporous photoanode. *Adv. Funct. Mater.* **2021**, *31* (8), 2008656.
(27) Chung, H. Y.; Toe, C. Y.; Chen, W.; Wen, X.; Wong, R. J.; Amal, R.; Abdi, F. F.; Ng, Y. H. Manipulating the fate of charge carriers with tungsten concentration: Enhancing photoelectrochemical water oxidation of Bi_2WO_6. *Small* **2021**, *17* (35), No. 2102023.
(28) Li, Z.; Zhang, Z.; Wang, L.; Meng, X. Bismuth chromate (Bi_2CrO_6): A promising semiconductor in photocatalysis. *J. Catal.* **2020**, *382*, 40−48.
(29) Lou, S. N.; Scott, J.; Iwase, A.; Amal, R.; Ng, Y. H. Photoelectrochemical water oxidation using a Bi_2MoO_6/MoO_3 heterojunction photoanode synthesised by hydrothermal treatment of an anodised MoO_3 thin film. *J. Mater. Chem. A* **2016**, *4* (18), 6964−6971.
(30) Wang, Z.-Q.; Wang, H.; Wu, X.-F.; Chang, T.-L. Oxygen vacancies and p-n heterojunction modified BiOBr for enhancing donor density and separation efficiency under visible-light irradiation. *J. Alloy. Compd.* **2020**, *834*, 155025.
(31) Liu, C.; Zhou, J.; Su, J.; Guo, L. Turning the unwanted surface bismuth enrichment to favourable $BiVO_4$/BiOCl heterojunction for enhanced photoelectrochemical performance. *Appl. Catal., B* **2019**, *241*, 506−513.
(32) Ye, K.-H.; Chai, Z.; Gu, J.; Yu, X.; Zhao, C.; Zhang, Y.; Mai, W. BiOI-$BiVO_4$ photoanodes with significantly improved solar water splitting capability: p−n junction to expand solar adsorption range and facilitate charge carrier dynamics. *Nano Energy* **2015**, *18*, 222−231.
(33) Spasibko, K. Y.; Kopylov, D. A.; Krutyanskiy, V. L.; Murzina, T. V.; Leuchs, G.; Chekhova, M. V. Multiphoton effects enhanced due to ultrafast photon-number fluctuations. *Phys. Rev. Lett.* **2017**, *119* (22), 223603.
(34) Mu, Y.; Wang, T.; Zhang, J.; Meng, C.; Zhang, Y.; Kou, Z. Single-atom catalysts: Advances and challenges in metal-support interactions for enhanced electrocatalysis. *Electrochem. Energy Rev.* **2022**, *5* (1), 145−186.
(35) Simmons, R. M.; Finer, J. T.; Chu, S.; Spudich, J. A. Quantitative measurements of force and displacement using an optical trap. *Biophys. J.* **1996**, *70*, 1813−1822.
(36) Ruiz Puigdollers, A.; Schlexer, P.; Tosoni, S.; Pacchioni, G. Increasing oxide reducibility: The role of metal/oxide interfaces in the formation of oxygen vacancies. *ACS Catal.* **2017**, *7* (10), 6493−6513.
(37) Honkala, K.; Häkkinen, H. Au adsorption on regular and defected thin MgO(100) films supported by Mo. *J. Phys. Chem. C* **2007**, *111* (11), 4319−4327.
(38) Giordano, L.; Goniakowski, J.; Pacchioni, G. Properties of MgO(100) ultrathin layers on Pd(100): Influence of the metal support. *Phys. Rev. B* **2003**, *67* (4), 045410.
(39) Giordano, L.; Goniakowski, J.; Pacchioni, G. Characteristics of Pd adsorption on the MgO(100) surface: Role of oxygen vacancies. *Phys. Rev. B* **2001**, *64* (7), 075417.
(40) Ammal, S. C.; Heyden, A. Modeling the noble metal/TiO_2 (110) interface with hybrid DFT functionals: A periodic electrostatic embedded cluster model study. *J. Chem. Phys.* **2010**, *133* (16), 164703.
(41) Pan, J. B.; Wang, B. H.; Wang, J. B.; Ding, H. Z.; Zhou, W.; Liu, X.; Zhang, J. R.; Shen, S.; Guo, J. K.; Chen, L.; Au, C. T.; Jiang, L. L.; Yin, S. F. Activity and stability boosting of an oxygen-vacancy-rich $BiVO_4$ photoanode by NiFe-MOFs thin layer for water oxidation. *Angew. Chem., Int. Ed.* **2021**, *60* (3), 1433−1440.
(42) Wang, M.; Ye, M.; Iocozzia, J.; Lin, C.; Lin, Z. Plasmon-mediated solar energy conversion via photocatalysis in noble metal/semiconductor composites. *Adv. Sci.* **2016**, *3* (6), 1600024.
(43) Cui, J.; Daboczi, M.; Regue, M.; Chin, Y.-C.; Pagano, K.; Zhang, J.; Isaacs, M. A.; Kerherve, G.; Mornto, A.; West, J.; Gimenez, S.; Kim, J.-S.; Eslava, S. 2D bismuthene as a functional interlayer between $BiVO_4$ and NiFeOOH for enhanced oxygen-evolution photoanodes. *Adv. Funct. Mater.* **2022**, *32* (44), 2207136.
(44) Huang, Y.; Zhu, Y.; Chen, S.; Xie, X.; Wu, Z.; Zhang, N. Schottky junctions with Bi cocatalyst for taming aqueous phase N_2 reduction toward enhanced solar ammonia production. *Adv. Sci.* **2021**, *8* (6), 2003626.
(45) Lei, R.; Tang, Y.; Yan, S.; Qiu, W.; Guo, Z.; Tian, X.; Wang, Q.; Zhang, K.; Ju, S.; Yang, S.; Wang, X. De-pinning fermi level and accelerating surface kinetics with an ALD finish boost the fill factor of $BiVO_4$ photoanodes to 44%. *Small* **2024**, *20* (7), No. 2306513.
(46) Klahr, B.; Gimenez, S.; Fabregat-Santiago, F.; Hamann, T.; Bisquert, J. Water oxidation at hematite photoelectrodes: the role of surface states. *J. Am. Chem. Soc.* **2012**, *134* (9), 4294−4302.
(47) Klahr, B.; Gimenez, S.; Fabregat-Santiago, F.; Bisquert, J.; Hamann, T. W. Electrochemical and photoelectrochemical investigation of water oxidation with hematite electrodes. *Energy Environ. Sci.* **2012**, *5* (6), 7626.
(48) Zhang, H.; Li, D.; Byun, W. J.; Wang, X.; Shin, T. J.; Jeong, H. Y.; Han, H.; Li, C.; Lee, J. S. Gradient tantalum-doped hematite homojunction photoanode improves both photocurrents and turn-on voltage for solar water splitting. *Nat. Commun.* **2020**, *11* (1), 4622.
(49) Trześniewski, B. J.; Digdaya, I. A.; Nagaki, T.; Ravishankar, S.; Herraiz-Cardona, I.; Vermaas, D. A.; Longo, A.; Gimenez, S.; Smith, W. A. Near-complete suppression of surface losses and total internal quantum efficiency in $BiVO_4$ photoanodes. *Energy Environ. Sci.* **2017**, *10* (6), 1517−1529.
(50) Ye, S.; Shi, W.; Liu, Y.; Li, D.; Yin, H.; Chi, H.; Luo, Y.; Ta, N.; Fan, F.; Wang, X.; Li, C. Unassisted photoelectrochemical cell with multimediator modulation for solar water splitting exceeding 4% solar-to-hydrogen efficiency. *J. Am. Chem. Soc.* **2021**, *143* (32), 12499−12508.
(51) Nishiyama, H.; Yamada, T.; Nakabayashi, M.; Maehara, Y.; Yamaguchi, M.; Kuromiya, Y.; Nagatsuma, Y.; Tokudome, H.; Akiyama, S.; Watanabe, T.; Narushima, R.; Okunaka, S.; Shibata, N.; Takata, T.; Hisatomi, T.; Domen, K. Photocatalytic solar hydrogen production from water on a 100-m^2 scale. *Nature* **2021**, *598* (7880), 304−307.
(52) Ahmet, I. Y.; Ma, Y.; Jang, J.-W.; Henschel, T.; Stannowski, B.; Lopes, T.; Vilanova, A.; Mendes, A.; Abdi, F. F.; van de Krol, R. Demonstration of a 50 cm^2 $BiVO_4$ tandem photoelectrochemical-photovoltaic water splitting device. *Sustain. Energy Fuels* **2019**, *3* (9), 2366−2379.

https://doi.org/10.1021/jacs.6c01306
J. Am. Chem. Soc. XXXX, XXX, XXX−XXX

(53) Patil Kunturu, P.; Lavorenti, M.; Bera, S.; Johnson, H.; Kinge, S.; van de Sanden, M. C. M.; Tsampas, M. N. Scaling up $BiVO_4$ photoanodes on porous Ti transport layers for solar hydrogen production. *ChemSusChem* **2024**, *17* (2), No. e202300969.
(54) Yao, X.; Wang, D.; Zhao, X.; Ma, S.; Bassi, P. S.; Yang, G.; Chen, W.; Chen, Z.; Sritharan, T. Scale-up of $BiVO_4$ photoanode for water splitting in a photoelectrochemical cell: issues and challenges. *Energy Technol.* **2018**, *6* (1), 100−109.

https://doi.org/10.1021/jacs.6c01306
J. Am. Chem. Soc. XXXX, XXX, XXX−XXX